Supercrystal Engineering of Atomically Precise Gold Nanoparticles Promoted by Surface Dynamics

Qiaofeng Yao[1,2#], Lingmei Liu[3#], Sami Malola[4#], Meng Ge[5], Hongyi Xu[5], Zhennan Wu[1], Tiankai Chen[1], Yitao Cao[1], María Francisca Matus[4], Antti Pihlajamäki[4], Yu Han[6]*, Hannu Häkkinen[4,7]* and Jianping Xie[1,2]*

[1] Department of Chemical and Biomolecular Engineering, National University of Singapore, 4 Engineering Drive 4, Singapore 117585.

[2] Joint School of National University of Singapore and Tianjin University, International Campus of Tianjin University, Binhai New City, Fuzhou, China 350207.

[3] Multi-scale Porous Materials Center, Institute of Advanced Interdisciplinary Studies & School of Chemistry and Chemical Engineering, Chongqing University, Chongqing, 400044 P. R. China.

[4] Department of Physics, Nanoscience Center, University of Jyväskylä, FI-40014 Jyväskylä, Finland.

[5] Department of Materials and Environmental Chemistry, Stockholm University, SE-106 91 Stockholm, Sweden.

[6] Advanced Membranes and Porous Materials Center, Physical Sciences and Engineering Division, King Abdullah University of Science and Technology (KAUST), Thuwal 23955-6900, Saudi Arabia.

[7] Department of Chemistry, Nanoscience Center, University of Jyväskylä, FI-40014 Jyväskylä, Finland.

[#] These authors contributed equally to this work.

* Corresponding authors:

Yu Han, email: yu.han@kaust.edu.sa;

Hannu Häkkinen, email: hannu.j.hakkinen@jyu.fi

Jianping Xie, email: chexiej@nus.edu.sg

Abstract

The controllable packing of functional nanoparticles (NPs) into crystalline lattices is of interest in the development of NP-based materials. Here we demonstrate that the size, morphology, and symmetry of such supercrystals can be tailored by adjusting the surface dynamics of their constituent NPs. In the presence of excess tetraethylammonium cations, atomically precise $[Au_{25}(SR)_{18}]^-$ NPs (where SR is a thiolate ligand) can be crystallized into micrometer-sized hexagonal rod-like supercrystals, rather than as face-centered-cubic superlattices otherwise. Experimental characterization supported by theoretical modeling show that the rod-like crystals consist of polymeric chains in which Au_{25} NPs are held together by linear RS–[Au(I)–SR]$_4$ inter-particle linker. This linker is formed by conjugation of two dynamically detached SR–[Au(I)–SR]$_2$ protecting motifs from adjacent Au_{25} particles, and stabilized by a combination of CH···π and ion-pairing interactions between tetraethylammonium cations and SR ligands. The symmetry, morphology, and size of the resulting supercrystals can be systematically tuned by changing the concentration and type of tetraalkylammonium cations.

In the past few decades, the scope of crystalline materials has been remarkably expanded by using functional inorganic nanoparticles (NPs) as "programmable atom equivalents (PAEs)"[1-6]. Assembling monodisperse NPs into supercrystals has proven an effective way to modulate their intrinsic optical, electronic, magnetic, and catalytic activities through inter-particle coupling and crystal order coherence[4, 7-12], which can be promoted by diverse inter-particle interactions, including electrostatic interaction[6], depletion force[13], metallophilicity[8, 14], H-bond[15], and biorecognition interaction[16, 17]. In these documented successful attempts, inorganic NPs are generally regarded as hard (or slightly deformable) spheres, and their stacking symmetry is determined by their "static" surface patterns. Intriguingly, recent advances in atomically precise nanoscience show marked structural dynamics in/between inorganic core and organic protecting shell of NPs[18-21], although such dynamics has not yet been utilized to regulate the assembly behavior of NPs.

Atomically precise thiolated gold NPs or "nanoclusters" with a specific chemical formula $[Au_m(SR)_n]^q$ (m, n, and q are the number of gold atoms, thiolate ligands (SR), and net charge per particle, respectively) are an emerging family of ultra-small metal particles (core size <3 nm)[22, 23]. They can be synthesized and characterized with atomic precision. Recent advances in X-ray crystallography suggest a core-shell structure of $[Au_m(SR)_n]^q$ NPs with well-ordered atomic (metal) and molecular (ligand) arrangement patterns at different structural hierarchies, reminiscent of biomolecules like proteins[3, 24]. Such well-ordered intra- and inter-particle arrangement patterns are largely sustained by supramolecular interactions, such as CH···π interaction[3], metallophilicity[8, 14], and conformational matching of protecting motifs[24]. More importantly, the diffusion of intra-particle metal atoms and the migration of surface protecting motifs have been observed in

many $[Au_m(SR)_n]^q$ or their alloy NPs, suggesting the existence of structural dynamics at the molecular and atomic levels[19-21]. In addition, $[Au_m(SR)_n]^q$ NPs also exhibit size- and structure-sensitive physicochemical properties (e.g., HOMO-LUMO transitions[25, 26], luminescence[27-29], and intrinsic chirality[30]), which provide a good channel to probe the growth fundamentals of supercrystals.

Herein, we demonstrate that surface dynamics of Au NPs can serve to regulate the structure (e.g., size, shape, and packing symmetry) of the NP supercrystals. Atomically precise $[Au_{25}(p\text{-MBA})_{18}]^-$ (*p*-MBA = *para*-mercaptobenzoic acid) are used as model NPs, and tetraalkylammonium cations are used to regulate their surface dynamics via a combination of CH···π and ion-pairing interactions (central panel, Fig. 1a). In the absence of any tetraalkylammonium cations, the deprotonated NPs tend to pack as hard spheres in cubic (face-centered-cubic or FCC-like) superlattices, forming a macroscopic octahedral supercrystal shape (top panels, Fig. 1a). However, the introduction of a suitable tetraalkylammonium cation (e.g., tetraethylammoniun (TEA^+)) as structure-directing agent will give rise to NP polymers connected by SR-$[Au(I)\text{-}SR]_4$ linkers, which are formed by the asymmetric conjugation of two dynamically detached SR-$[Au(I)\text{-}SR]_2$ motifs from adjacent NPs. Close-packing of as-formed NP polymers leads to micro-meter-sized hexagonal rod-like supercrystals (bottom panels, Fig. 1a). The NP packing symmetry and morphology of these NP metamaterials can be tuned by the dosage and size of related tetraalkylammonium cations. This work demonstrates a facile method for engineering the morphology and symmetry of crystalline NP metamaterials at the micro-meter size regime and highlights the importance of surface dynamics of NPs in determining their assembly behavior.

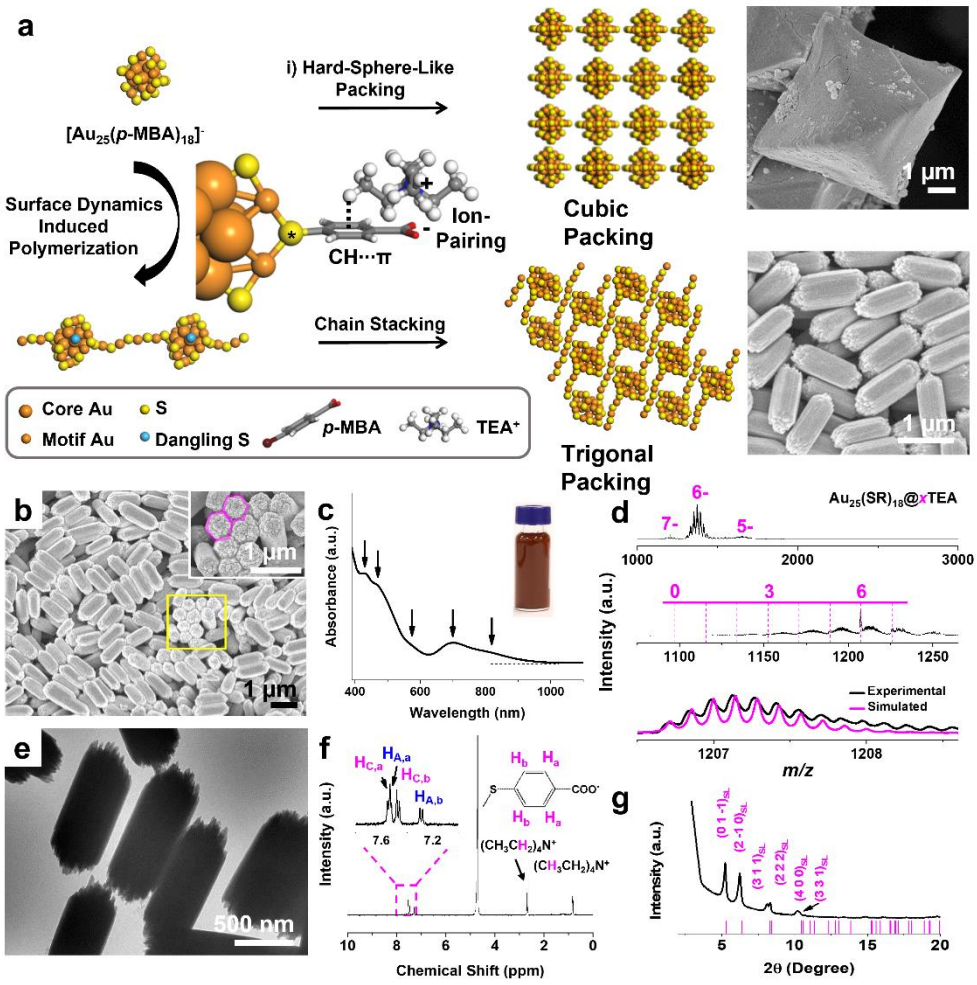

Figure 1. Crystallization of [Au$_{25}$(*p*-MBA)$_{18}$]$^{-}$ nanoparticles into hexagonal rod-like supercrystals. (a) Schematic illustration of the crystallization of hard-sphere-like [Au$_{25}$(*p*-MBA)$_{18}$]$^{-}$ (*p*-MBA = *para*-mercaptobenzoic acid) NPs into either face-centered-cubic (FCC) superlattices and octahedral crystals (top) or, in the presence of excess tetraethylammonium cations (TEA^{+}), a R-3m superlattice and hexagonal rod-like supercrystals (bottom). In the presence of excess TEA^{+}, two SR–[Au(I)–SR]$_2$ fragments dynamically detached from adjacent Au$_{25}$ particles are stabilized into an inter-particle linker through a combination of CH···π and ion-pairing interactions between TEA^{+} and *p*-

MBA ligands, favouring a one-dimensional alignment of the particles. The asymmetric detachment of SR–[Au(I)–SR]$_2$ fragments leaves a dangling S (blue sphere) on the surface of each nanoparticle. Right panels: a typical field-emission scanning electron microscopy (FESEM) image of octahedral supercrystals (top) and hexagonal rod-like supercrystals (bottom). (b) FESEM image of hexagonal rod-like supercrystals; the inset is a zoomed-in view of the squared area, where the magenta hexagons outline the cross-sections of two rods. (c) Ultraviolet-visible (UV-vis) absorption spectrum of hexagonal rod-like supercrystals re-dissolved in water; the inset is a digital photo of supercrystals dispersed in dimethyl sulfoxide (DMSO). (d) electrospray ionization (ESI) mass spectrum of redissolved hexagonal rod-like supercrystals; the top panel is wide-range mass spectrum, where the charges of particle peaks are labelled; the middle panel is zoomed-in view of particle peaks carrying 7- charge, where the number of TEA^+ bonded to individual $[Au_{25}(p\text{-}MBA)_{18}]^-$ is indicated by the dashed droplines; the black and magenta lines in the bottom panel are experimental and simulated isotope patterns of $[Au_{25}(p\text{-MBA})_{18}@6TEA - 12H]^{7-}$, respectively. (e) Transmission electron microscopy (TEM) images of hexagonal rod-like supercrystals. (f) ^{1}H-NMR spectra of the hexagonal rod-like supercrystals re-dissolved in deuterated water; left inset is zoomed-in view of the aromatic region of ^{1}H-NMR spectrum, and right inset depicts the hydrogen atoms of *p*-MBA ligands in different chemical environments. (g) Powder X-ray diffraction (PXRD) pattern of hexagonal rod-like supercrystals, where the Miller indexes of superlattice (SL) planes are labeled. The examined hexagonal-rod-like supercrystals were formed at the molar ratio of TEA^+ and Li^+, $R_{TEA/Li} = 3/1$.

Results and discussion

Synthesis of $[Au_{25}(p\text{-MBA})_{18}]^-$ supercrystals. Freshly prepared $[Au_{25}(p\text{-MBA})_{18}]^-$ NPs (Supplementary Fig. 1 and Supplementary Note 1)[31] were patched with TEA^+ on their surfaces — small Li^+ was used as co-cations (with a molar ratio of TEA^+/Li^+, $R_{TEA/Li} = 3/1$) to effectively neutralize the surface charges of NPs against the bulky hydrocarbon tails of TEA^+ — followed by crystallization via a selective evaporation approach in a dual-solvent system of water and dimethyl sulfoxide (DMSO)[32]. As-produced precipitates can be re-dispersed in its mother liquid or fresh DMSO by shaking briefly (inset, Fig. 1c), which suggests the successful formation of micro-meter-sized supercrystals. Field-emission scanning electron microscopy (FESEM) and transmission electron microscopy (TEM) analyses (Fig. 1b and 1e) on the supercrystals manifest a rod-like morphology with a typical longitudinal size of 1.25 ± 0.15 μm (Supplementary Fig. 2, 100 rods counted), an aspect ratio (*r*) of 2.45, and a hexagonal cross-section (inset, Fig. 1b). Powder X-ray diffraction (PXRD) pattern (Fig. 1g) of the rod-like supercrystals shows clearly discernable peaks in the 2θ regime of 2-20˚, indicating their highly crystalline nature.

In sharp contrast to the well-maintained structural architectures in DMSO, the as-obtained hexagonal rod-like supercrystals can be completely dissociated into discrete $[Au_{25}(p\text{-MBA})_{18}]^-$ NPs in water. The combined UV-vis absorption spectroscopy (Fig. 1c) and electrospray ionization mass spectrometry (ESI-MS, Fig. 1d) analyses suggest that the size- and structure-uncompromised $[Au_{25}(p\text{-MBA})_{18}]^-$ NPs are recovered from the dissociated supercrystals. The ESI-MS spectrum also suggests a good structural stability for $Au_{25}(p\text{-MBA})_{18}$@6TEA, where markedly high population of $Au_{25}(p\text{-MBA})_{18}$@6TEA is observed in the particle peaks carrying 7- charge. The quantitative ^1H nuclear magnetic

resonance (^{1}H-NMR, Fig. 1f) analysis manifests 6.01 ± 0.19 (three independent samples tested) TEA^+ molecules bonded to individual particle (i.e., x = 6 in Au_{25}(p-MBA)$_{18}$@xTEA). More details about molecular characterization of the re-dissolved hexagonal rod-like supercrystals can be found in Supplementary Note 2 and Supplementary Fig. 3.

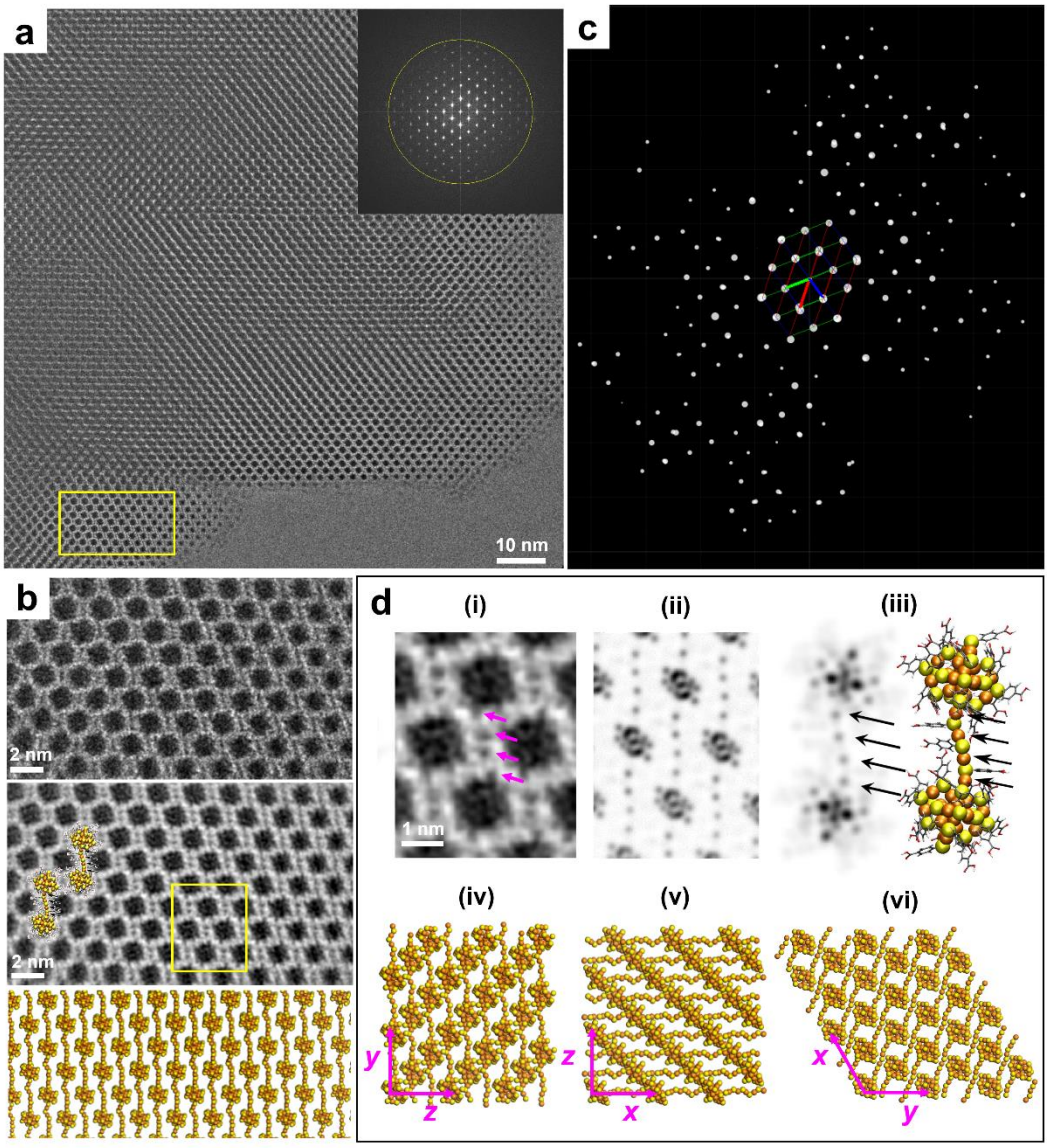

Figure 2. Packing structure determination of hexagonal rod-like supercrystals. (a) Bright-field ultralow-dose TEM image of rod-like supercrystals; the inset (top right) shows the fast Fourier transfer pattern. (b) Top panel, zoomed-in view of the area in (a) outlined with a dashed yellow rectangle; middle panel, corresponding contrast transfer function (CTF)-corrected image; bottom panel, structural model. (c) Reconstructed 3D electron diffraction lattice of rod-like supercrystals. (d) Particle packing models of rod-like supercrystals along $[1\ -1\ -1]_{SL}$ zone axis. (i), enlarged view of the outlined area of the middle panel in (b); (ii), simulated TEM image reproducing that in panel (i); (iii), simulated TEM image (left) and structure model (right) of the $[Au_{25}(SR)_{18}]^-$ dimer formed through SR-[Au(I)-SR]$_4$ inter-particle linker (SR = thiolate), where the Au atoms in the inter-particle linker are indicated by the arrows; (iv–vi) show the R-3m superlattices of $[Au_{25}(p\text{-MBA})_{18}]^-$ viewed along *x* (iv), *y* (v), and *z* (vi) axes. Color code: Au, orange; S, yellow; C, grey; O, red; H, light grey; the hydrocarbon tails of *p*-MBA ligands are only shown in panel (iii) of (d) for clarity purpose.

Packing and atomic structure of NPs in the supercrystals. The supercrystal structure formed by the TEA^+-bonded $[Au_{25}(p\text{-MBA})_{18}]^-$ NPs (i.e., $Au_{25}(p\text{-MBA})_{18}$@6TEA) was examined by 3D electron diffraction (3D ED) technique. The 3D ED datasets collected from hexagonal rod-like supercrystals (Fig. 2c and Supplementary Fig. 4) show a R-3m unit cell with cell parameters of $a = b = 27.7$ Å, $c = 23.4$ Å, $\alpha = \beta = 90^\circ$, and $\gamma = 120^\circ$. With the determined unit cell, the main diffraction peaks at $2\theta = 5.22^\circ$, 6.25°, 8.08°, 8.33°, 10.21°, and 10.37° can be assigned to the superlattice (SL) planes of $(0\ 1\ -1)_{SL}$, $(2\ -1\ 0)_{SL}$, $(3\ 1\ 1)_{SL}$, $(2\ 2\ 2)_{SL}$, $(4\ 0\ 0)_{SL}$, and $(3\ 3\ 1)_{SL}$, respectively (Fig. 1g).

In order to better understand the structural details, high-resolution images of the supercrystals consisting of $[Au_{25}(p\text{-MBA})_{18}]^-$ NPs were obtained using a recently developed ultralow-dose TEM technique, which can effectively avoid electron beam-induced structural changes/damages[33, 34]. The bright-field ultralow-dose TEM image (the total electron dose as low as ~15 $e^{-}\cdot Å^{-2}$) taken at the Scherzer focus along the $[1\ -1\ -1]_{SL}$ incidence (Fig. 2a) shows a highly ordered structure composed of monodisperse NPs. The corresponding fast Fourier transfer pattern is shown as an inset in Fig. 2a, and the yellow circle indicates the frequency of 2.5 Å. Based on the structure of the unit cell solved by the 3D ED, we indexed the projected direction of this typical ultralow-dose TEM image as $[1\ -1\ -1]_{SL}$ zone axis. We then selected an ultrathin area from Fig. 2a (marked by the square) for image processing, which was performed by correcting the effect of contrast transfer function (CTF) of the objective lens. The CTF-corrected image approximately corresponds to the projected electrostatic potential of the structure and is therefore directly interpretable. In the CTF-corrected image (middle panel, Fig. 2b), black dots with a diameter of 0.98 nm are observed with a rhombus packing structure. The size of the black dots nicely matches with the core diameter of $[Au_{25}(SR)_{18}]^-$ measured by X-ray crystallography[25, 35], which means each black dot represents one $[Au_{25}(SR)_{18}]^-$ NP. Moreover, this conclusion is supported by high-angle annular dark field scanning transmission electron microscopy (HAADF-STEM) (Supplementary Fig. 5). More intriguingly, regular dark spots are observed between adjacent NPs (arrowed in panel (i) of Fig. 2d), suggesting an unusual packing mode in the supercrystals (*vide infra*).

The near-atomic-resolution ultralow-dose TEM images (Fig. 2b) provide a good opportunity to investigate the atomic structure of individual $[Au_{25}(p\text{-MBA})_{18}]^-$ NP in the

supercrystals. Since there is currently no atom-level crystal structure of $[Au_{25}(p\text{-MBA})_{18}]^-$, we analyze the structure based on two potential candidates: the crystal structure of $[Au_{25}(PET)_{18}]^-$ with an organothiolate ligand (i.e., 2-phenylethanethiolate (PET), hereinafter referred to as **isomer 1)**[25, 35], and the recently theoretically suggested[36] and experimentally observed (in gas-phase)[37] topological isomer of $[Au_{25}(PET)_{18}]^-$ (**isomer 2**). Theoretical models of the corresponding structures with the *p*-MBA ligand, optimized by density functional theory (DFT) calculations (using the GPAW software[38]; see technical details in Methods and Supplementary Note 3), are shown in Supplementary Fig. 6b and 6c. Simulated TEM images of the models projected from a number of spatial directions were compared to the TEM data shown in Fig. 2b by using the Complex Wavelet Structural Similarity (CW-SSIM) method (details in Supplementary Note 3)[39]. The results (Supplementary Fig. 7 and 8) clearly indicate that the **isomer 2** could be excluded from further consideration to build a 3D atomic model of the Au_{25} NP supercrystals.

Using the $[Au_{25}(SR)_{18}]^-$ **isomer 1** structure, we built models implying a crystal of packed single-particle chains or polymers of Au_{25} NPs, where the linkers in the polymers consist of four Au atoms with bridging thiolates (yielding the observed dark spots in TEM images in Fig. 2b, 2d, and Supplementary Fig. 6). Formation of such four-Au-atom linker bridged by thiolates can be envisioned by considering the atomic structure of **isomer 1** (Supplementary Fig. 6b). It should be reminded that in the "divide-and-protect" scheme[40], the chemical composition of $[Au_{25}(SR)_{18}]^-$ can be written as $[Au_{13}@(SR\text{-}[Au(I)\text{-}SR]_2)_6]^-$, where the icosahedral Au_{13} core is protected by six SR-$[Au(I)\text{-}SR]_2$ motifs (Supplementary Fig. 1c). Considering the dynamics of their surface structure, two adjacent Au_{25} NPs can react by opening one end of the SR-$[Au(I)\text{-}SR]_2$ motif via breaking a Au-S bond on a core-

type SR (i.e., SR_C as illustrated in Supplementary Fig. 3a), followed by conjugation of the opened motifs from the adjacent NP. Therefore, two geometries for such polymeric linkers exist: one having a RS-SR bond in the middle in a symmetric configuration (i.e., [SR-Au(I)]$_2$-RS-SR-[Au(I)-SR]$_2$), and the other one having an asymmetric geometry with a SR-[Au(I)-SR]$_4$ linker connecting the NPs (Supplementary Fig. 9 and 10c). DFT calculations on periodic NP polymer model (Supplementary Fig. 10a and 10b) imply that the asymmetrically linked NP polymer is energetically preferred over the symmetric one, with the energy difference of ~0.75 eV per simulation unit cell. Optimal inter-particle distance was estimated to be about 2.3 – 2.5 nm (Supplementary Fig. 10b), which is close to the experimentally observed inter-particle distance along the $[1\ 1\ 0]_{SL}$ direction (i.e., 2.75 nm). An experimental support for this result was obtained from the Raman scattering spectrum of the hexagonal rod-like supercrystals, where no S-S bond fingerprints were observed in the regime of 400-550 cm^{-1} (Supplementary Fig. 10d)[41]. It should be noted that the seminal work on the reaction chemistry of Au NPs has theoretically proposed different structural models based on the inter-particle SR-[Au(I)-SR]$_2$ linkers, accounting for the Au_{25} NP dimers captured by ESI-MS in gas phase[42]. We excluded those models in our DFT calculations due to their obviously shorter inter-particle distance.

Using the asymmetric linkage model, a 3D model crystal from the packed $[Au_{25}(SR)_{18}]^-$ NP polymers was built upon orienting the polymeric chains along the $[1\ 1\ 0]_{SL}$ direction. This 3D model (bottom panel, Fig. 2b) shows a good match with the CTF-corrected ultralow-dose TEM image in Fig. 2b (middle panel). Close to the atomic resolution, the zoom-in comparison of experimental, simulated TEM images, and structural model of $[Au_{25}(SR)_{18}]^-$ NP dimer further strengthens the model, as shown in panel (i)-(iii) of Fig. 2d.

Typical views of the R-3m superlattice along different axis are illustrated in Fig. 2d (panel (iv)-(vi)). The accuracy of as-proposed packing model has also been verified by the ultralow-dose TEM images taken along the $[1\ 0\ 0]_{SL}$ direction (Supplementary Fig. 11).

Besides the formation of 1D polymeric chain along the $[1\ 1\ 0]_{SL}$ direction, the formation of R-3m superlattice is also prompted by the close packing of as-formed polymeric chains of $[Au_{25}(p\text{-MBA})_{18}]^-$, which does not involve the formation of the SR-[Au(I)-SR]$_4$ linkers. As shown in Supplementary Fig. 12a, the hexagonal arrangement of NPs in the $(1\ -1\ -1)_{SL}$ plane can be formed by the close packing of $[1\ 1\ 0]_{SL}$ oriented NP chains in an ABAB stacking manner. In this 2D stacking pattern, each NP has four nearest NPs with a characteristic inter-particle distance of 1.76 nm, which is the shortest inter-particle distance observed in the R-3m superlattice (Supplementary Fig. 12a). Subsequent layer-by-layer stacking of as-described 2D particle planes along the $[1\ -1\ -1]_{SL}$ direction with an inter-particle distance of 1.76 nm produces a 3D R-3m superlattice. Of note, the preferential growth direction of hexagonal rod-like supercrystals is shown by large-scale ultralow-dose TEM analysis as $[1\ -1\ 2]_{SL}$ (Supplementary Fig. 12b), corresponding well to the chain closest-packing direction in the superlattice (Supplementary Fig. 12a). It should be noted that the ordered 1D alignment of atomically precise metal NPs have been previously made possible via metallophilic interactions (e.g., Au-Au and Ag-Au-Ag)[8, 14, 43], disulfide bonds[44], and atomic/molecular linkers[45, 46]. However, the alignment of Au NPs by virtue of their surface dynamics has not yet been reported. The aforementioned packing mode of NP polymers also suggests different packing density within and vertical to the $(1\ -1\ -1)_{SL}$ plane, which allows us to exfoliate the as-formed hexagonal rod-like supercrystals into

layered NP assemblies (Supplementary Fig. 13 and Supplementary Note 4), reminiscent of the layer-by-layer exfoliation of 2D materials such as graphene and black phosphorus[47, 48].

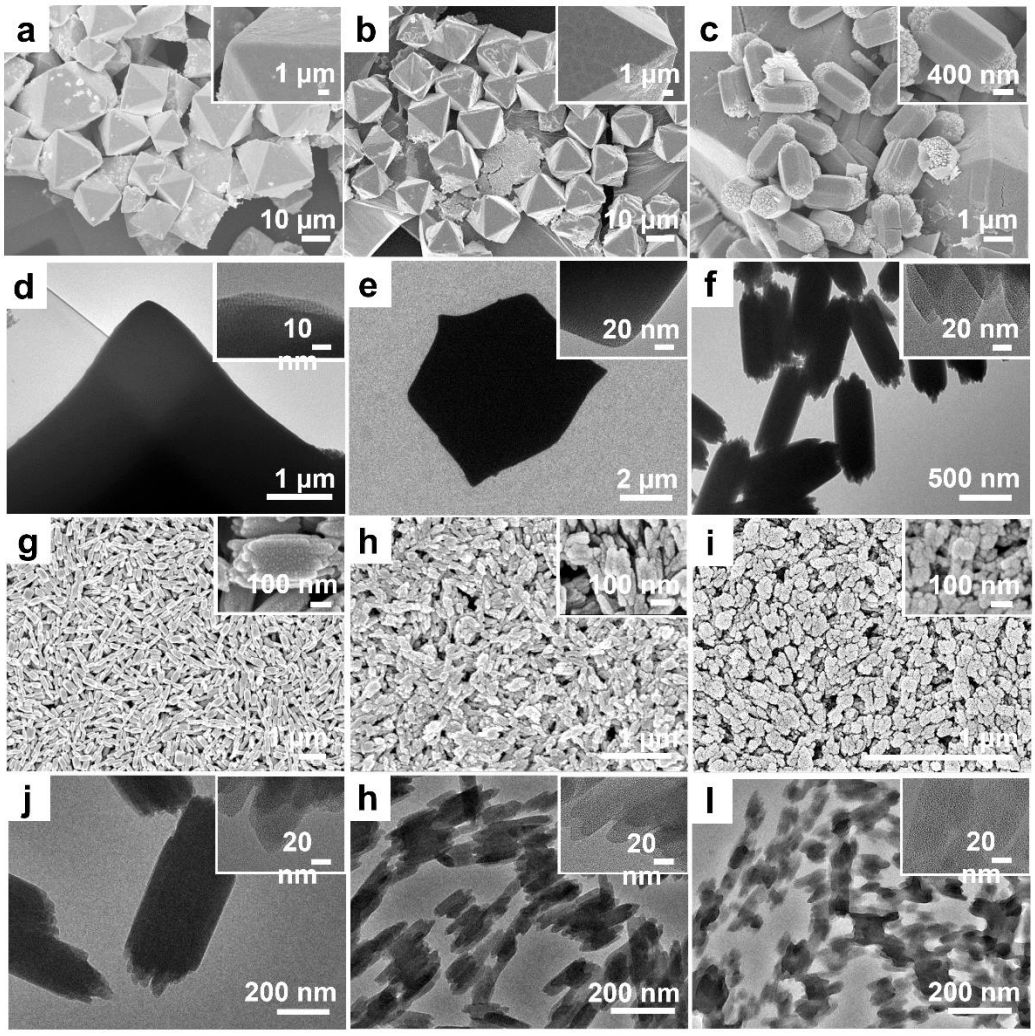

Figure 3. Crystallization habit of $[Au_{25}(p\text{-MBA})_{18}]^-$ nanoparticles in the presence of various ratios of tetraalkylammonium and lithium cations. (a-c) FESEM and (d-f) TEM images of $[Au_{25}(p\text{-MBA})_{18}]^-$ NPs crystallized at varied ratios of TEA^+ and Li^+, $R_{TEA/Li}$ = 0/4 (a, d), 1/3 (b, e), and 2/2 (c, f). (g-i) FESEM and (j-l) TEM images of $[Au_{25}(p\text{-MBA})_{18}]^-$ NPs crystallized at $R_{TEA/Li}$ = 3.5/0.5 (g, j), 3.75/0.25 (h, k), and 4/0 (i, l). Insets are zoom-in views of the corresponding EM images. The EM images suggest the

crystallization habits of NPs are tunable via altering the dosage of TEA^+, where ~1 nm dots observed in zoom-in TEM images indicate the supercrystals are packed by $[Au_{25}(p\text{-}MBA)_{18}]^-$ NPs.

Morphology engineering of the supercrystals. The use of structure-directing agent, TEA^+, is crucial for the formation of the hexagonal rod-like supercrystals. By changing the molar ratio of TEA^+ and alkaline metal co-cations (e.g., Li^+) while keeping other experimental conditions unchanged, the morphology of as-formed supercrystals could evolve from octahedron ($R_{TEA/Li}$ = 0/4, Fig. 3a and 3d; $R_{TEA/Li}$ = 1/3, Fig. 3b and 3e), via a mixture of octahedron and hexagonal rods ($R_{TEA/Li}$ = 2/2, Fig. 3c and 3f), to pure hexagonal rods ($R_{TEA/Li}$ = 3/1, Fig. 1b and 1e). This readily suggests that a threshold surface coverage of TEA^+ is required to trigger the formation of hexagonal rod-like supercrystals. Otherwise, the crystallization behavior of $[Au_{25}(p\text{-}MBA)_{18}]^-$ is predictable by the typical hard sphere model in the Li^+-rich surroundings, where the entropy effect tends to pack NPs into the FCC supercrystals with an octahedral morphology (Supplementary Fig. 14, 15 and Supplementary Note 5)[32]. It should be noted that similar formation of octahedral or concave-octahedral supercrystals has been observed for Cs^+-deprotonated $[Ag_{44}(p\text{-}MBA)_{30}]^{4-}$ NPs, which is governed by the entropy effects and electrostatic repulsion rather than the surface dynamics of NPs[32]. In contrast to modulating the crystalline phase, further increasing the dosage of TEA^+ can reduce the size of rod-like supercrystals while keeping their R-3m packing unchanged (Fig. 3g-3l, Supplementary Fig. 15-17 and Supplementary Note 5).

UV-vis absorption (Fig. 4a) and ESI-MS (Fig. 4b and 4c) spectra of the re-dissolved supercrystals confirm that the size of $[Au_{25}(p\text{-MBA})_{18}]^-$ NPs in the supercrystals remains unchanged regardless of the $R_{TEA/Li}$ values. More intriguingly, the extensive formation of rod-like supercrystals coincides with the dominance of $Au_{25}(p\text{-MBA})_{18}$@6TEA species in the ESI-MS spectra (Fig. 4c). This again suggests the improved structural stability of $Au_{25}(p\text{-MBA})_{18}$@6TEA and its pivotal role in the formation of R-3m superlattice. The crucial role of $Au_{25}(p\text{-MBA})_{18}$@6TEA can also be verified by ^{1}H-NMR analysis (Fig. 4d). All the peaks identified in Fig. 4d can be attributed to *p*-MBA anchored on the surface of $[Au_{25}(p\text{-MBA})_{18}]^-$ (Fig. 4f), TEA^+, and residual solvent (i.e., DMSO and ethanol; Fig. 4e). Quantitative analysis based on the integral peak intensity suggests that the number of TEA^+ bonded to individual $[Au_{25}(p\text{-MBA})_{18}]^-$ NP increases with the increase of $R_{TEA/Li}$ and reaches a plateau of $Au_{25}(p\text{-MBA})_{18}$@6TEA at $R_{TEA/Li}$ = 3/1 or higher (Supplementary Fig. 18).

Molecular interaction between TEA^+ and $[Au_{25}(p\text{-MBA})_{18}]^-$. To investigate the preferential bonding sites of TEA^+ on the surface of $[Au_{25}(p\text{-MBA})_{18}]^-$ NPs, we zoomed-in the aromatic region of the ^{1}H-NMR spectra. It can be seen from Fig. 4f that the four types of chemically distinct hydrogen of *p*-MBA ligands (see Supplementary Fig. 3a) exhibit different chemical shifts (δ) in response to increasing dosage of TEA^+. With the increase of $R_{TEA/Li}$, the resonances of $H_{A,a}$ (denoting H_a atom in SR_A), $H_{A,b}$, and $H_{C,b}$ exhibit significant downfield shifts, while those of $H_{C,a}$ only show marginal downfield shifts (arrows in Fig. 4f). The marginal downfield shifts of $H_{C,a}$ readily indicate that TEA^+ would preferentially bond to the $–COO^-$ groups of SR_A instead of SR_C. This ion-pairing-induced

downfield shift of $H_{A,a}$ resonance is also supported by the gradual upfield shift of H resonances of TEA^+ with its elevating concentration (Fig. 4e). Therefore, the significant downfield shifts of $H_{A,b}$ and $H_{C,b}$ should be attributed to their close proximity to the Au(0) core of $[Au_{25}(p\text{-MBA})_{18}]^-$ NPs, whose electronic structure is sensitive to TEA^+ bonding, as evidenced by the red-shifted absorption peak at ~690 nm (Supplementary Fig. 19). It has become increasingly known that the CH···π interactions are effective in maintaining the ligand arrangement patterns at the intra-particle level and assembly fashions at the inter-particle level of atomically precise metal NPs[3, 49]. Therefore, we hypothesized that the CH···π interaction is another important attribute (compared to the ion-pairing interaction) that can tether TEA^+ on the surface of $[Au_{25}(p\text{-MBA})_{18}]^-$ NPs (panel (iv), Fig. 1a). This assertion is experimentally supported by 2D ^1H-^1H nuclear Overhauser effect spectroscopy (NOESY) analysis on the NP solution before crystallization (Supplementary Fig. 20), indicating that the alkyl chains of TEA^+ are spatially close to the phenyl rings of *p*-MBA ligands. Therefore, by combining the ion-pairing and CH···π interactions, six TEA^+ cations can selectively bind to the six SR_A in individual $[Au_{25}(p\text{-MBA})_{18}]^-$ NP. Anchoring bulky TEA^+ on the surface of $[Au_{25}(p\text{-MBA})_{18}]^-$ NPs can then induce strains in the SR-[Au(I)-SR]$_2$ protecting motifs, thereby enhancing their dynamics on the particle surface. The enhanced dynamics of the SR-[Au(I)-SR]$_2$ motifs promotes their partial detachment from the NP surface and further conjugation into the inter-particle SR-[Au(I)-SR]$_4$ linker, which can provide a unique mechanism for construction of polymeric NP chains in the self-assembly/crystallization scenarios. The enhanced surface dynamics induced by selective TEA^+ bonding is also experimentally supported by tandem mass spectrometry (MS/MS) analysis (Supplementary Fig. 21-71 and Supplementary Note 6).

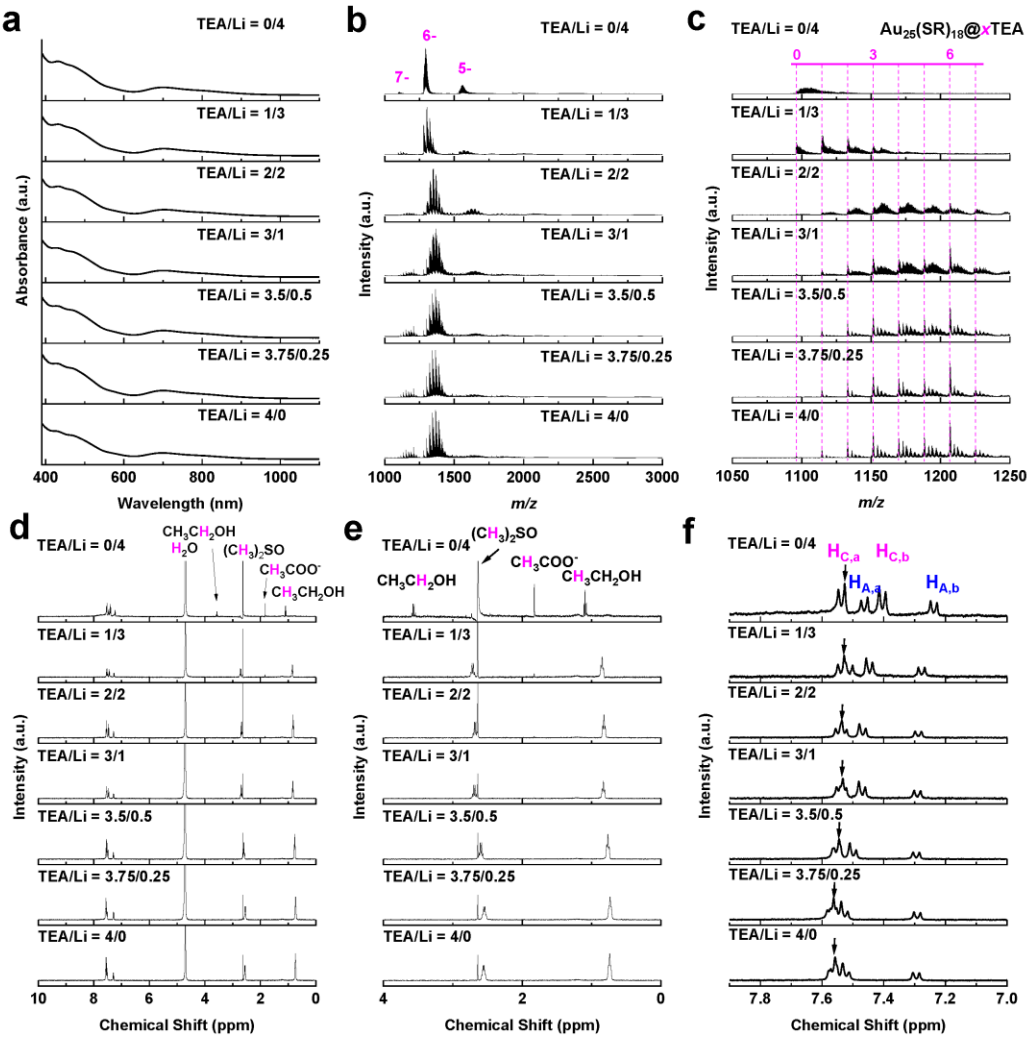

Figure 4. Characterization of the supercrystals' building blocks. (a) UV-vis absorption and (b) wide-range ESI-MS spectra of $[Au_{25}(p\text{-MBA})_{18}]^-$ NPs crystallized at varied ratios of TEA^+ and Li^+, $R_{TEA/Li}$ = 0/4, 1/3, 2/2, 3/1, 3.5/0.5, 3.75/0.25, and 4/0; the charge numbers of particle ions are labelled above the corresponding peaks in the ESI-MS spectra. (c) zoom-in view of 7- cluster peaks in (b), where the dashed droplines are eye guides of *x* values in $Au_{25}(SR)_{18}@x$TEA. (d) ^{1}H-NMR spectra of $[Au_{25}(p\text{-MBA})_{18}]^-$ NPs crystallized at varied $R_{TEA/Li}$. (e, f) Zoom-in views of the aliphatic (e) and aromatic (f) region of ^{1}H-

NMR spectra shown in (d). The molecule-level characterization indicates the building blocks of rod-like supercrystals are $Au_{25}(SR)_{18}$@6TEA NPs, where TEA^+ are preferentially anchored on the apex-type SR ligands of NPs.

To investigate the molecular details of the interaction between the tetraalkylammonium cations and the linked $[Au_{25}(p\text{-MBA})_{18}]^-$ NPs, we carried out extensive molecular dynamics (MD) simulations on short (dimeric and tetrameric) polymer models of $[Au_{25}(p\text{-MBA})_{18}]^-$ NPs in the aqueous solution in the presence of tetramethylammonium (TMA^+)/TEA^+/tetrapropylammonium (TPA^+) using GROMACS software[50]. Fig. 5a shows a representative snapshot from 50 ns MD trajectory of $[Au_{25}(p\text{-MBA})_{18}]^-$ dimer with TEA^+ cations, which can visualize the CH···π interactions between *p*-MBA ligands and TEA^+. The MD simulations by including designed amount of TEA^+ in the simulation cell (see more details in Methods and Supplementary Note 7) suggest that the total number of CH···π interactions in the simulation cell remains rather similar irrespective of the cation concentration (12 vs. 36 TEA^+ in the cell, Fig. 5b), but, remarkably, the TEA^+ has a clear effect on stabilizing the inter-particle distance (Fig. 5d, 5e and Supplementary Note 7). The inter-particle distance suitable for the growth of Au_{25} NP polymers was achieved in the presence of adequate TEA^+, despite TMA^+ gives rise to the greatest number of CH···π interactions (Fig. 5c). The optimal effects of TEA^+ on the formation of $[Au_{25}(p\text{-MBA})_{18}]^-$ NP polymer and thus rod-like supercrystals are supported by our crystallization experiments of $[Au_{25}(p\text{-MBA})_{18}]^-$ NPs in the presence of TMA^+, TPA^+, and tetrabutylammonium (TBA^+), which ubiquitously yield octahedral supercrystals (Supplementary Fig. 72-76). Finally, MD simulations of the longer tetrameric polymer

model of $[Au_{25}(p\text{-MBA})_{18}]^-$ NPs (Supplementary Fig. 77) show that the longer NP polymers are very flexible in solution, and the crystallization must proceed by gradually increasing (weak) interactions between adjacent polymeric chains when the solvent evaporates, eventually rigidifying the packed chains with a short inter-chain distance (1.76 nm; Supplementary Fig. 12a). Moreover, in order to evaluate the relative importance of the ion-pairing reactions and CH···π interactions in stabilizing the SR-[Au(I)-SR]$_4$ inter-particle linkers, we compared short-range Coulomb (as a proxy of ion-paring interactions) and Lennard-Jones (as a proxy of CH···π interactions) energies (Supplementary Fig. 78 and Supplementary Table 1). The consistently more negative value of the latter throughout the concerned simulation time (50 ns, with 12 or 36 TEA^+ in the simulation cell) unambiguously supports the dominant role of the CH···π interactions in stabilizing the as-mentioned inter-particle linkers.

Growth of truncated rhombus flake-like supercrystals. With a good understanding of the importance of TEA^+ in the formation of hexagonal rod-like supercrystals, we also studied the effects of co-cations on the crystallization of $[Au_{25}(p\text{-MBA})_{18}]^-$ NPs. The data not only shows a descending trend of supercrystal size with the increase of co-cation size, but also suggests that TMA^+ can competitively (against TEA^+) bond to $[Au_{25}(p\text{-MBA})_{18}]^-$ during their crystallization process (Supplementary Fig. 79-89 and Supplementary Note 8). Our analysis of crystallization kinetics (Supplementary Fig. 90-97 and Supplementary Note 9) further suggests fast nucleation and slow growth kinetics for the hexagonal rod-like supercrystals ($R_{TEA/Li}$ = 3/1), and slow nucleation and fast growth kinetics for the octahedral supercrystals ($R_{TEA/Li}$ = 0/4).

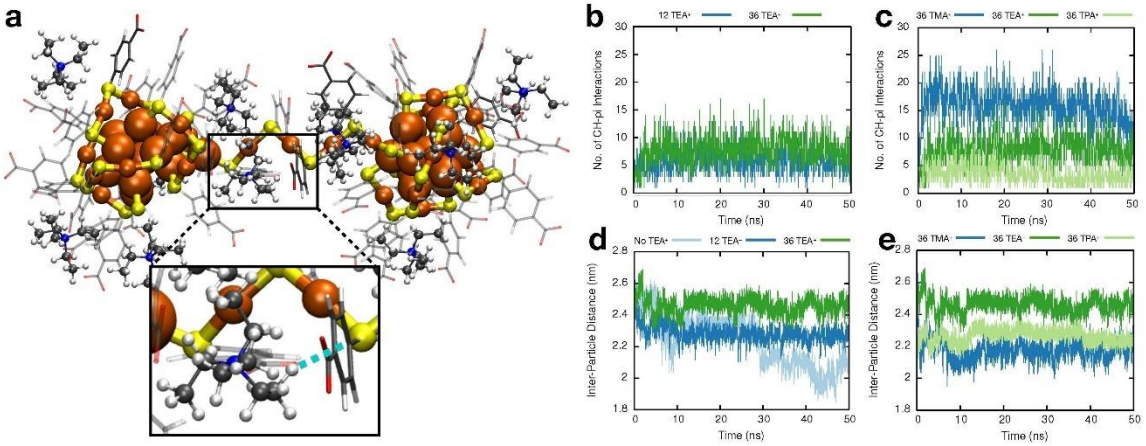

Figure 5. Effects of tetraalkylammonium cations on the stability of $[Au_{25}(p\text{-MBA})_{18}]^-$ dimer. (a) Representative snapshot from 50 ns molecular dynamics (MD) trajectory of $[Au_{25}(p\text{-MBA})_{18}]^-$ dimer formed by the assistance of TEA^+, showing the CH···π interactions between *p*-MBA^- ligands and TEA^+. Color code and representation: Au atoms in the Au_{13} core, large orange spheres;; Au atoms in the protecting motifs, small orange spheres; *p*-MBA ligands, thick sticks; TEA^+ cations, balls and sticks; CH···π interactions, dashed cyan lines; S, yellow; C, grey; O, red; N, blue; H, light grey. (b, c) Total number of CH···π interactions and (d, e) inter-particle distances in $[Au_{25}(p\text{-MBA})_{18}]^-$ dimer formed at varied dosages of TEA^+ (b, d) and for varied tetraalkylammonium cations (c, e): tetramethylammonium (TMA^+), TEA^+, and tetrapropylammonium (TPA^+). The molecular dynamics analyses demonstrate TEA^+ is the optimized tetraalkylammonium cation for stabilizing the $[Au_{25}(p\text{-MBA})_{18}]^-$ dimer.

Based on the above kinetics knowledge, we can further fine-tune the morphology of supercrystals. In the crystallization solution containing TEA^+ and TMA^+, increasing the ratio of competitive cation TMA^+ is expected to slow down the growth kinetics of rod-like supercrystals, allowing supercrystals to have more relaxing time to evolve into a well-

defined shape. Therefore, we conducted the crystallization of $[Au_{25}(p\text{-MBA})_{18}]^-$ with the molar ratio of TEA^+/TMA^+, $R_{TEA/TMA}$ = 2/2. The as-formed supercrystals exhibit a well-defined morphology of truncated rhombus flake (Fig. 6a and 6b). The HAADF-STEM image (Fig. 6c-6e) and P-XRD spectrum (Supplementary Fig. 98d) suggest that these flake-like supercrystals adopt R-3m superlattices, similar to the rod-like supercrystals formed at $R_{TEA/Li}$ = 3/1. UV-vis absorption (Supplementary Fig. 98a), ESI-MS (Supplementary Fig. 98b), and ^{1}H-NMR (Supplementary Fig. 98c) spectra of the re-dissolved supercrystals confirm that the building blocks for the flake-like supercrystals are size-unchanged $[Au_{25}(p\text{-MBA})_{18}]^-$ NPs. Moreover, reducing $R_{TEA/TMA}$ further to 1/3 can shape supercrystals into rhombus prisms (Supplementary Fig. 99i), while crystallization experiment using TPA^+ and TBA^+ as co-cations in a similar $R_{TEA/CoM}$ regime produces rod-like supercrystals exclusively (Supplementary Fig. 99), corroborating the tunability of crystallization kinetics of $[Au_{25}(p\text{-MBA})_{18}]^-$ NPs by TMA^+.

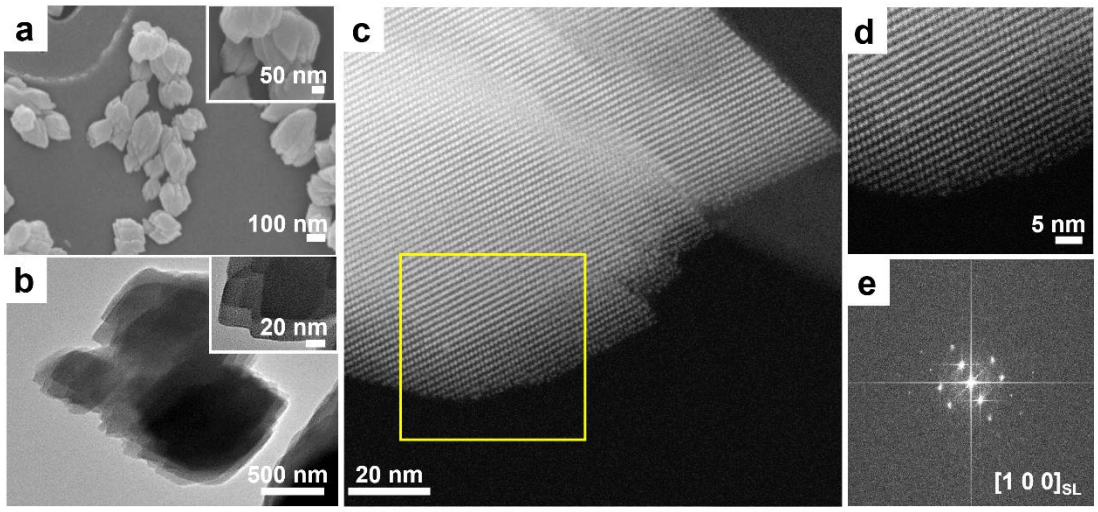

Figure 6. Shaping supercrystals into truncated rhombus flakes. (a) FESEM, (b) TEM, and (c) HAADF-STEM images viewed along $[1\ 0\ 0]_{SL}$ direction of $[Au_{25}(p\text{-MBA})_{18}]^-$ supercrystals formed in the presence of TEA^+ and TMA^+ with a molar ratio of $R_{TEA/TMA}$ =

2/2. (d) Enlarged view of the outlined area of (c). (e) Fast Fourier transfer pattern corresponding to (d)/outlined area of (c). By changing the ratio of TEA^+ and TMA^+, the shape of the supercrystals can be tuned from rod to rhombus flake.

Conclusion

In summary, we have developed a structure-directing-agent-assisted method to tune the symmetry, morphology, and size of Au NP supercrystals. This strategy relies on the surface modulation capability of TEA^+ cation, where a combination of CH···π and ion-pairing interactions between *p*-MBA ligands and TEA^+ stabilizes the dynamic, partial detachment of SR-[Au(I)-SR]$_2$ protecting motifs from the surface of $[Au_{25}(p\text{-MBA})_{18}]^-$ NPs. The conjugation of such partially detached SR-[Au(I)-SR]$_2$ motifs between adjacent NPs gives rise to an SR-[Au(I)-SR]$_4$ inter-particle linker, aligning $[Au_{25}(p\text{-MBA})_{18}]^-$ NPs into 1D polymeric chains. The close packing of as-formed NP polymeric chains produces hexagonal rod-like supercrystals. Such hexagonal rod-like supercrystals adopt a trigonal R-3m space group, which is in sharp contrast to the FCC octahedral supercrystals of $[Au_{25}(p\text{-MBA})_{18}]^-$ formed without TEA^+. The control of crystallization kinetics by TMA^+ can further shape the supercrystals into truncated rhombus flakes and rhombus prisms. Extensive theoretical work has provided molecule-level understanding of the internal structure of the supercrystals, starting from image analysis of TEM data to an atom-level model of the linked $[Au_{25}(p\text{-MBA})_{18}]^-$ NPs. This facilitates DFT calculations and MD simulations on the atomic structure, cation-ligand interactions, and the dynamic stabilization of the linked NP polymers, indicating TEA^+ as the optimal structure-directing cation. This work not only demonstrates the usefulness of tetraalkylammonium cations in

tailoring the symmetry, morphology, and size of NP supercrystals, but also exemplifies the importance of molecule-level surface dynamics of Au NPs to their assembly and crystallization behavior.

Acknowledgements

We acknowledge the financial support of the Ministry of Education, Singapore (Academic Research Grant R-279-000-580-112 (J.X) and R-279-000-538-114 (J.X.)) and National Natural Science Foundation of China (22071174 (J.X.)). The theoretical work at University of Jyväskylä was supported by the Academy of Finland (grants 292352 (H.H.), 318905 (H.H.), 319208 (H.H.), and H.H.'s Academy Professorship). The computations were done at the CSC computing center in Finland and in the FGCI - Finnish Grid and Cloud Infrastructure (persistent identifier urn:nbn:fi:research-infras-2016072533). The funders had no role in study design, data collection and analysis, decision to publish or preparation of the manuscript.

Author contributions

J.X. and Y.H. supervised the experimental work. J.X. and Q.Y. conceived the idea and designed the experiment. Q.Y., L.L. M.G. and H.X. carried out the experiments and characterizations. Z.W., T.C. and Y.C. contributed to data interpretation and theory development. H.H. supervised the theoretical and computational work. A.P. performed the image similarity analysis correlating Au_{25} NP models to the TEM data, S.M. performed DFT computations of the single NPs and linked NP models, M.F.M. performed the MD

simulations of the linked NP models in aqueous solution. All authors contributed to manuscript writing.

Competing interests

The authors declare no competing interests.

References

1. Zhang, C., *et al.* A general approach to DNA-programmable atom equivalents. *Nat. Mater.* **12**, 741-746 (2013).

2. Shevchenko, E. V., Talapin, D. V., Kotov, N. A., O'Brien, S. & Murray, C. B. Structural diversity in binary nanoparticle superlattices. *Nature* **439**, 55-59 (2006).

3. Zeng, C., Chen, Y., Kirschbaum, K., Lambright, K. J. & Jin, R. Emergence of hierarchical structural complexities in nanoparticles and their assembly. *Science* **354**, 1580-1584 (2016).

4. Huang, R.-W., *et al.* Hypersensitive dual-function luminescence switching of a silver-chalcogenolate cluster-based metal–organic framework. *Nat. Chem.* **9**, 689-697 (2017).

5. Takano, S. & Tsukuda, T. Chemically modified gold/silver superatoms as artificial elements at nanoscale: design principles and synthesis challenges. *J. Am. Chem. Soc.* **143**, 1683-1698 (2021).

6. Kalsin, A. M., Fialkowski, M., Paszewski, M., Smoukov, S. K., Bishop, K. J. M. & Grzybowski, B. A. Electrostatic self-assembly of binary nanoparticle crystals with a diamond-like lattice. *Science* **312**, 420-424 (2006).

7. Boles, M. A., Engel, M. & Talapin, D. V. Self-assembly of colloidal nanocrystals: from intricate structures to functional materials. *Chem. Rev.* **116**, 11220-11289 (2016).

8. De Nardi, M., *et al.* Gold nanowired: a linear $(Au_{25})_n$ polymer from Au_{25} molecular clusters. *ACS Nano* **8**, 8505-8512 (2014).

9. Zhao, M., *et al.* Ambient chemical fixation of CO_2 using a robust Ag_{27} cluster-based two-dimensional metal–organic framework. *Angew. Chem. Int. Ed.* **59**, 20031-20036 (2020).

10. Ross, M. B., Ku, J. C., Vaccarezza, V. M., Schatz, G. C. & Mirkin, C. A. Nanoscale form dictates mesoscale function in plasmonic DNA–nanoparticle superlattices. *Nat. Nanotechnol.* **10**, 453-458 (2015).

11. Huang, J.-H., Wang, Z.-Y., Zang, S.-Q. & Mak, T. C. W. Spontaneous resolution of chiral multi-thiolate-protected Ag_{30} nanoclusters. *ACS Cent. Sci.* **6**, 1971-1976 (2020).

12. Chen, T., *et al.* Crystallization-induced emission enhancement: a novel fluorescent Au-Ag bimetallic nanocluster with precise atomic structure. *Sci. Adv.* **3**, e1700956 (2017).

13. Bodnarchuk, M. I., Kovalenko, M. V., Heiss, W. & Talapin, D. V. Energetic and entropic contributions to self-assembly of binary nanocrystal superlattices: temperature as the structure-directing factor. *J. Am. Chem. Soc.* **132**, 11967-11977 (2010).

14. Hossain, S., *et al.* Understanding and designing one-dimensional assemblies of ligand-protected metal nanoclusters. *Mater. Horiz.* **7**, 796-803 (2020).

15. Desireddy, A., *et al.* Ultrastable silver nanoparticles. *Nature* **501**, 399-402 (2013).

16. Tian, Y., Zhang, Y., Wang, T., Xin, H. L., Li, H. & Gang, O. Lattice engineering through nanoparticle–DNA frameworks. *Nat. Mater.* **15**, 654-661 (2016).

17. Auyeung, E., *et al.* DNA-mediated nanoparticle crystallization into Wulff polyhedra. *Nature* **505**, 73-77 (2014).

18. Cao, Y., *et al.* Reversible isomerization of metal nanoclusters induced by intermolecular interaction. *Chem* **7**, 2227-2244 (2021).

19. Zheng, K., Fung, V., Yuan, X., Jiang, D.-e. & Xie, J. Real time monitoring of the dynamic intracluster diffusion of single gold atoms into silver nanoclusters. *J. Am. Chem. Soc.* **141**, 18977-18983 (2019).

20. Salassa, G., Sels, A., Mancin, F. & Bürgi, T. Dynamic nature of thiolate monolayer in $Au_{25}(SR)_{18}$ nanoclusters. *ACS Nano* **11**, 12609-12614 (2017).

21. Barrabés, N., Zhang, B. & Bürgi, T. Racemization of chiral $Pd_2Au_{36}(SC_2H_4Ph)_{24}$: doping increases the flexibility of the cluster surface. *J. Am. Chem. Soc.* **136**, 14361-14364 (2014).

22. Jin, R., Zeng, C., Zhou, M. & Chen, Y. Atomically precise colloidal metal nanoclusters and nanoparticles: fundamentals and opportunities. *Chem. Rev.* **116**, 10346-10413 (2016).

23. Chakraborty, I. & Pradeep, T. Atomically precise clusters of noble metals: emerging link between atoms and nanoparticles. *Chem. Rev.* **117**, 8208-8271 (2017).

24. Li, Y., Zhou, M., Song, Y., Higaki, T., Wang, H. & Jin, R. Double-helical assembly of heterodimeric nanoclusters into supercrystals. *Nature* **594**, 380-384 (2021).

25. Zhu, M., Aikens, C. M., Hollander, F. J., Schatz, G. C. & Jin, R. Correlating the crystal structure of a thiol-protected Au_{25} cluster and optical properties. *J. Am. Chem. Soc.* **130**, 5883-5885 (2008).

26. Lopez-Acevedo, O., Kacprzak, K. A., Akola, J. & Häkkinen, H. Quantum size effects in ambient CO oxidation catalysed by ligand-protected gold clusters. *Nat. Chem.* **2**, 329-334 (2010).

27. Liao, L., *et al.* An unprecedented kernel growth mode and layer-number-odevity-dependent properties in gold nanoclusters. *Angew. Chem. Int. Ed.* **59**, 731-734 (2020).

28. Wu, Z., *et al.* Unraveling the impact of gold(I)–thiolate motifs on the aggregation-induced emission of gold nanoclusters. *Angew. Chem. Int. Ed.* **59**, 9934-9939 (2020).

29. Zheng, J., Nicovich, P. R. & Dickson, R. M. Highly fluorescent noble-metal quantum dots. *Annu. Rev. Phys. Chem.* **58**, 409-431 (2007).

30. Dolamic, I., Knoppe, S., Dass, A. & Bürgi, T. First enantioseparation and circular dichroism spectra of Au_{38} clusters protected by achiral ligands. *Nat. Commun.* **3**, 798 (2012).

31. Yao, Q., *et al.* Understanding seed-mediated growth of gold nanoclusters at molecular level. *Nat. Commun.* **8**, 927 (2017).

32. Yao, Q., *et al.* Counterion-assisted shaping of nanocluster supracrystals. *Angew. Chem. Int. Ed.* **54**, 184-189 (2015).

33. Zhang, D., *et al.* Atomic-resolution transmission electron microscopy of electron beam–sensitive crystalline materials. *Science* **359**, 675-679 (2018).

34. Liu, L., *et al.* Imaging defects and their evolution in a metal–organic framework at sub-unit-cell resolution. *Nat. Chem.* **11**, 622-628 (2019).

35. Heaven, M. W., Dass, A., White, P. S., Holt, K. M. & Murray, R. W. Crystal structure of the gold nanoparticle $[N(C_8H_{17})_4][Au_{25}(SCH_2CH_2Ph)_{18}]$. *J. Am. Chem. Soc.* **130**, 3754-3755 (2008).

36. Matus, M. F., Malola, S., Kinder Bonilla, E., Barngrover, B. M., Aikens, C. M. & Häkkinen, H. A topological isomer of the $Au_{25}(SR)_{18}^{-}$ nanocluster. *Chem. Commun.* **56**, 8087-8090 (2020).

37. Kalenius, E., Malola, S., Matus, M. F., Kazan, R., Bürgi, T. & Häkkinen, H. Experimental confirmation of a topological isomer of the ubiquitous $Au_{25}(SR)_{18}$ cluster in the gas phase. *J. Am. Chem. Soc.* **143**, 1273-1277 (2021).

38. Enkovaara, J., *et al.* Electronic structure calculations with GPAW: a real-space implementation of the projector augmented-wave method. *J. Phys. Condens. Matter.* **22**, 253202 (2010).

39. Wang, Z. & Simoncelli, E. P. Translation insensitive image similarity in complex wavelet domain. In: *Proceedings. (ICASSP '05). IEEE International Conference on Acoustics, Speech, and Signal Processing, 2005.* **2**, 573-576 (2005).

40. Häkkinen, H., Walter, M. & Grönbeck, H. Divide and protect: capping gold nanoclusters with molecular gold−thiolate rings. *J. Phys. Chem. B* **110**, 9927-9931 (2006).

41. Price, R. C. & Whetten, R. L. Raman spectroscopy of benzenethiolates on nanometer-scale gold clusters. *J. Phys. Chem. B* **110**, 22166-22171 (2006).

42. Baksi, A., Chakraborty, P., Bhat, S., Natarajan, G. & Pradeep, T. $[Au_{25}(SR)_{18}]_2^{2-}$: a noble metal cluster dimer in the gas phase. *Chem. Commun.* **52**, 8397-8400 (2016).

43. Yuan, P., *et al.* Solvent-mediated assembly of atom-precise gold–silver nanoclusters to semiconducting one-dimensional materials. *Nat. Commun.* **11**, 2229 (2020).

44. Lahtinen, T., *et al.* Covalently linked multimers of gold nanoclusters Au_{102}(*p*-MBA)$_{44}$ and $Au_{\sim 250}$(*p*-MBA)$_n$. *Nanoscale* **8**, 18665-18674 (2016).

45. Liu, X., *et al.* $Ag_2Au_{50}(PET)_{36}$ nanocluster: dimeric assembly of $Au_{25}(PET)_{18}$ enabled by silver atoms. *Angew. Chem. Int. Ed.* **59**, 13941-13946 (2020).

46. Wen, Z.-R., Guan, Z.-J., Zhang, Y., Lin, Y.-M. & Wang, Q.-M. $[Au_7Ag_9(dppf)_3(CF_3CO_2)_7BF_4]_n$: a linear nanocluster polymer from molecular Au_7Ag_8 clusters covalently linked by silver atoms. *Chem. Commun.* **55**, 12992-12995 (2019).

47. Wang, C., *et al.* Monolayer atomic crystal molecular superlattices. *Nature* **555**, 231 (2018).

48. Bao, W., *et al.* Approaching the limits of transparency and conductivity in graphitic materials through lithium intercalation. *Nat. Commun.* **5**, 4224 (2014).

49. Huang, R.-W., *et al.* $[Cu_{81}(PhS)_{46}(t\text{BuNH}_2)_{10}(H)_{32}]^{3+}$ reveals the coexistence of large planar cores and hemispherical shells in high-nuclearity copper nanoclusters. *J. Am. Chem. Soc.* **142**, 8696-8705 (2020).

50. Van Der Spoel, D., Lindahl, E., Hess, B., Groenhof, G., Mark, A. E. & Berendsen, H. J. C. GROMACS: fast, flexible, and free. *J. Comput. Chem.* **26**, 1701-1718 (2005).

Methods

Synthesis of $[Au_{25}(p\text{-MBA})_{18}]^-$ Nanoparticles. $[Au_{25}(p\text{-MBA})_{18}]^-$ NPs were prepared according to a reported carbon monoxide (CO)-reduction method with some minor modifications[31]. Specifically, 50 mM *p*-MBA aqueous solution (10 mL, in 150 mM NaOH) and 50 mM $HAuCl_4$ aqueous solution (5 mL) were sequentially added to ultrapure water (238.75 mL), and the reaction mixture was stirred at 1,000 rpm for 5 min. After that, the pH value of the reaction mixture was adjusted to 10.5 by dropping 1 M NaOH aqueous solution. After stirring for another 30 min, a light-yellow solution of Au(I)-(*p*-MBA) complexes was formed. Subsequently, CO was bubbled into the reaction mixture at a flow rate of 100 mL per min for 2 min, to initiate the reduction of the Au(I)-(*p*-MBA) complexes. The reaction was allowed to proceed airtightly at room temperature (25 °C) under vigorous stirring (1,000 rpm) for 3 days. The reddish-brown solution obtained at the end of this procedure was collected as raw product.

The raw product was first concentrated 10 times by rotary evaporation (water bath temperature 40 °C, cooling temperature 4 °C, and rotation rate 160 rpm). After that, ethanol (double the volume of the concentrated NP solution) was added, followed by centrifugation at 12,000 rpm for 5 min. The resultant pellet was washed twice with ethanol and re-dissolved in water for further characterization (more details about the materials and characterization can be found in Supplementary Methods). The molar extinction coefficient of $[Au_{25}(p\text{-MBA})_{18}]^-$ NPs at their characteristic absorption of ~690 nm (ε_{690}) was determined to be 15.08 $mM^{-1}\cdot cm^{-1}$ using the equation $OD_{690} = \varepsilon_{690}\cdot l\cdot[NP]$, where OD_{690}, l, and [NP] are optical density of absorption at ~690 nm, length of light path (1 cm for our

apparatus), and concentration of Au_{25} NPs measured by inductively coupled plasma optical emission spectroscopy (ICP-OES), respectively.

Cyclic Cation Exchange of $[Au_{25}(p\text{-MBA})_{18}]^-$ Nanoparticles. The patching of TEA^+ and other cations on the particle surface was conducted by a cyclic cation exchange method. The freshly prepared $[Au_{25}(p\text{-MBA})_{18}]^-$ NP solution (raw product, 60 mL) was first concentrated 10 times by rotary evaporation (water bath temperature 40 °C, cooling temperature 4 °C, and rotation rate 160 rpm). After that, ethanol (double the volume of the concentrated NP solution) was added, followed by centrifugation at 12,000 rpm for 5 min. The precipitate was recovered and re-dissolved in 66.67 mM aqueous solution of acetate salt (1 mL, pH = 11.85) of desired cations (e.g., Li^+, Na^+, K^+, Cs^+, TMA^+, TEA^+, and TBA^+). For example, in a typical preparation of hexagonal rod-like supercrystals, an aqueous solution containing 66.67 mM acetate of TEA^+/Li^+ with a molar ratio, $R_{TEA/Li}$ = 3/1, was used as the cation-exchange solution. After incubating for 10 min under moderate stirring (600 rpm), five volumetric equivalent of ethanol was added, followed by centrifugation at 10,000 rpm for 5 min. The re-dissolution-centrifugation cycle was repeated two more times to complete the cation exchange process.

Synthesis of $[Au_{25}(p\text{-MBA})_{18}]^-$ Supercrystals. The supercrystals of $[Au_{25}(p\text{-MBA})_{18}]^-$ NPs were grown via a selective evaporation approach in a dual-solvent system[32]. Cation-exchanged $[Au_{25}(p\text{-MBA})_{18}]^-$ NPs (the target concentration of NPs was 0.50 mM) were re-dissolved in a mixture of DMSO/water (1/1, v/v) containing 33.33 mM (total cation concentration) of the designed cation or cation combination to form the crystallization solution. The crystallization solution was then placed in a vacuum oven at ~20 mbar and

50 °C to selectively remove water from the mixture. The evaporation usually lasted 1-2 days (depending on the cations used), and the solid supercrystals of $[Au_{25}(p\text{-MBA})_{18}]^-$ NPs can be collected from the bottom of the crystallization tube at the end of the procedure. For a typical growth of the hexagonal rod-like supercrystals, a crystallization solution containing 33.33 mM (total cation concentration) of TEA^+/Li^+ ($R_{TEA/Li}$ = 1/3) was subjected to vacuum treatment for 1 day. After that, the hexagonal rod-like supercrystals can be collected as dark red precipitates at the bottom of the crystallization tube. As-produced supercrystals can be redissolved in water, and the recovery rate of $[Au_{25}(p\text{-MBA})_{18}]^-$ NPs from supercrystals is measurable based on the ε_{690} in the UV-vis absorption spectra. A typical recovery of 88.7% or 91.7% was recorded for typical rod-like (formed at $R_{TEA/Li}$ = 3/1) or octahedral (formed at $R_{TEA/Li}$ = 1/3) supercrystals, respectively.

Density Functional Theory (DFT) Calculations. Density functional theory, as implemented in software GPAW[38] was used in optimization of model structures of **isomer 1** and **2** of $[Au_{25}(p\text{-MBA})_{18}]^-$ NPs, isolated linker molecules, 1D polymeric chain, and the full 3D crystal model of NPs. Structure optimizations were done using the PBE-functional[51] in real-space grids with grid spacing of 0.2 Å. Optimizations were stopped when the maximum force on each atom was below 0.05 $eV \cdot Å^{-1}$. The projector augmented wave (PAW) setups for Au included scalar-relativistic corrections. Various linker molecules were optimized as isolated units to study the effects of the charge and the ligand type on the conformation. For the 1D periodic NP polymers, consecutive optimizations were performed by decreasing the length of experimentally observed periodic unit cell in steps of 0.05 nm. Such optimizations were stopped when minimum energy and thus optimal

inter-particle distance were achieved. 1D NP polymers were calculated using both symmetric (featuring S-S bond) and asymmetric bonding modes. The 3D supercrystal model was optimized using the experimentally determined unit cell dimensions and constructed with asymmetric linkers only. Because of the system size, only Γ-point calculation was performed without k-point sampling. One TEA^+ cation was included per particle to neutralize the charge of the periodic 1D and 3D model structures. In all systems the TEA^+ cations were added to the vicinity of the ligand layer of NPs. The effects of cations and solvent were analyzed in more details using classical force field molecular dynamics (MD) simulations with non-periodic finite dimer and tetramer NP polymer systems.

Molecular Dynamics (MD) Simulations. To study the role of different tetraalkylammonium cations, such as TEA^+, TMA^+, and TPA^+ on the flexibility of the NP polymers, MD simulations were carried out with DFT-based models of finite dimer and tetramer in solvent.

The full systems containing the dimer or tetramer and the cation molecules were constructed with PACKMOL[52], and then optimized and dynamically simulated using GROMACS 2019 MD simulation package[50, 53], with an AMBER force field used for thiolated NPs[54]. The force field parameters for TEA^+, TMA^+, and TPA^+ cations were obtained using suitable available parameters of the Amber99sb-ildn[55] force field. The partial charges were optimized following the restrained electrostatic potential (RESP) charge fitting procedure recommended for Amber[56]. The geometry optimization and ESP calculations according to the Merz−Singh−Kollman scheme[57, 58] were performed with

Gaussian09[59] at a B3LYP/6-31G* level of theory. Atomic charges were fitted to the obtained potential in a two-stage RESP fit procedure with Ambertools12[60]. All systems were simulated in a cubic simulation box solvated with TIP3P water[61], with all *p*-MBA groups deprotonated[62] (according to the experimental conditions of pH = 11.85). Sodium ions were added to neutralize the systems. The SETTLE algorithm was used to constrain the internal degrees of freedom of the water molecules[63]. Energy minimizations were carried out by using the steepest descent algorithm, followed by a short equilibration consisting of 1 ns NVT ensemble (constant number of particles, volume, and temperature) at 200 K and 1 ns NPT (constant number of particles, pressure, and temperature) at 298.15 K and 1 bar pressure with position restraints on dimer and TEA^+/TMA^+/TPA^+ cations. Afterwards, 50 ns of production simulations were performed for each system. A leapfrog Verlet integrator with 1 fs time step, a velocity-rescale thermostat with a reference temperature of 298.15 K and a coupling time constant of 0.1 ps[64], a 1.0 nm Lennard−Jones cutoff with dispersion correction for energy and pressure, periodic boundary conditions (PBC), Particle-mesh Ewald (PME) method with a 1.0 nm cutoff and 0.12 nm grid spacing[65], and Berendsen barostat with a reference pressure of 1 bar and coupling time constant of 1 ps[66] were used. For improved performance, the lengths of covalent bonds containing hydrogens were constrained with the LINCS algorithm[67].

All trajectories were analyzed in Visual Molecular Dynamics (VMD)[68]. The number of CH···π interactions[69] between *p*-MBA^- ligands and TEA^+/TMA^+/TPA^+ cations of each system over the simulated times was estimated by using an in-house tcl script.

Data availability

The authors declare that all the data supportive to the conclusions of this work are available in the paper and its Supplementary Information. Source data are provided in Source Data or Supplementary Data files. Additional simulation data are also available from the authors on reasonable request.

Additional information

Supplementary information is available for this paper at http://

51. Perdew, J. P., Burke, K. & Ernzerhof, M. Generalized gradient approximation made simple. *Phys. Rev. Lett.* **77**, 3865-3868 (1996).

52. Martínez, L., Andrade, R., Birgin, E. G. & Martínez, J. M. PACKMOL: A package for building initial configurations for molecular dynamics simulations. *J. Comput. Chem.* **30**, 2157-2164 (2009).

53. GROMACS 2019, https://www.gromacs.org/.

54. Pohjolainen, E., Chen, X., Malola, S., Groenhof, G. & Häkkinen, H. A unified AMBER-compatible molecular mechanics force field for thiolate-protected gold nanoclusters. *J. Chem. Theory Comput.* **12**, 1342-1350 (2016).

55. Lindorff-Larsen, K., *et al*. Improved side-chain torsion potentials for the Amber ff99SB protein force field. *Proteins Struct. Funct. Bioinforma.* **78**, 1950-1958 (2010).

56. Bayly, C. I., Cieplak, P., Cornell, W. & Kollman, P. A. A well-behaved electrostatic potential based method using charge restraints for deriving atomic charges: the RESP model. *J. Phys. Chem.* **97**, 10269-10280 (1993).

57. Singh, U. C. & Kollman, P. A. An approach to computing electrostatic charges for molecules. *J. Comput. Chem.* **5**, 129-145 (1984).

58. Besler, B. H., Merz Jr., K. M. & Kollman, P. A. Atomic charges derived from semiempirical methods. *J. Comput. Chem.* **11**, 431-439 (1990).

59. Frisch, M. J., *et al.* Gaussian 09. Gaussian, Inc; Wallingford, CT 32, 5648 (2009).

60. Case, D. A., *et al.* AMBER 12. University of California, San Francisco; San Francisco, CA (2012).

61. Jorgensen, W. L., Chandrasekhar, J., Madura, J. D., Impey, R. W. & Klein, M. L. Comparison of simple potential functions for simulating liquid water. *J. Chem. Phys.* **79**, 926-935 (1983).

62. Koivisto, J., *et al.* Acid–base properties and surface charge distribution of the water-soluble Au_{102}(*p*MBA)$_{44}$ nanocluster. *J. Phys. Chem. C* **120**, 10041-10050 (2016).

63. Miyamoto, S. & Kollman, P. A. Settle: An analytical version of the SHAKE and RATTLE algorithm for rigid water models. *J. Comput. Chem.* **13**, 952-962 (1992).

64. Bussi, G. & Parrinello, M. Stochastic thermostats: comparison of local and global schemes. *Comput. Phys. Commun.* **179**, 26-29 (2008).

65. Darden, T., York, D. & Pedersen, L. Particle mesh Ewald: an *N*·log(N) method for Ewald sums in large systems. *J. Chem. Phys.* **98**, 10089-10092 (1993).

66. Berendsen, H. J. C., Postma, J. P. M., Gunsteren, W. F. v., DiNola, A. & Haak, J. R. Molecular dynamics with coupling to an external bath. *J. Chem. Phys.* **81**, 3684-3690 (1984).

67. Hess, B., Bekker, H., Berendsen, H. J. C. & Fraaije, J. G. E. M. LINCS: a linear constraint solver for molecular simulations. *J. Comput. Chem.* **18**, 1463-1472 (1997).

68. Humphrey, W., Dalke, A. & Schulten, K. VMD: visual molecular dynamics. *J. Mol. Graph.* **14**, 33-38 (1996).

69. Chakraborty, P., *et al.* Exploration of CH···π interactions involving the π-system of pseudohalide coligands in metal complexes of a Schiff-base ligand. *CrystEngComm* **17**, 4680-4690 (2015).